

A PRECISE ESTIMATE OF THE RADIUS OF THE EXOPLANET HD 149026b FROM *SPITZER* PHOTOMETRY

PHILIP NUTZMAN¹, DAVID CHARBONNEAU^{1,5}, JOSHUA N. WINN², HEATHER A. KNUTSON¹, JONATHAN J. FORTNEY³,
MATTHEW J. HOLMAN¹, AND ERIC AGOL⁴

¹ Harvard-Smithsonian Center for Astrophysics, 60 Garden St., Cambridge, MA 02138, USA; pnutzman@cfa.harvard.edu

² Department of Physics, and Kavli Institute for Astrophysics and Space Research, Massachusetts Institute of Technology, Cambridge, MA 02139, USA

³ Department of Astronomy and Astrophysics, UCO/Lick Observatory, University of California, Santa Cruz, CA 95064, USA

⁴ Department of Astronomy, University of Washington, Box 351580, Seattle, WA 98195, USA

Received 2008 May 6; accepted 2008 October 20; published 2009 February 18

ABSTRACT

We present *Spitzer* 8 μm transit observations of the extrasolar planet HD 149026b. At this wavelength, transit light curves are weakly affected by stellar limb darkening, allowing for a simpler and more accurate determination of planetary parameters. We measure a planet–star radius ratio of $R_p/R_\star = 0.05158 \pm 0.00077$, and in combination with ground-based data and independent constraints on the stellar mass and radius, we derive an orbital inclination of $i = 85^\circ.4^{+0.9}_{-0.8}$ and a planet radius of $R_p = 0.755 \pm 0.040 R_J$. These measurements further support models in which the planet is greatly enriched in heavy elements.

Key words: planetary systems – techniques: photometric

1. INTRODUCTION

Much attention has been lavished on the transiting extrasolar planet HD 149026b (Sato et al. 2005) due to its potential to directly test models of planet formation. The planet’s small observed radius for its mass implies that an extraordinary fraction of its mass (roughly 2/3) is in the form of heavy elements (Sato et al. 2005; Fortney et al. 2006; Burrows et al. 2007). The discovery of a metal-laden planet orbiting a very metal-rich host star ([Fe/H] = 0.36; Sato et al. 2005) strongly suggests that core accretion (e.g., Pollack et al. 1996) plays a role in forming giant planets. If, however, most of the heavy elements reside in the planet’s core, then HD 149026b would possess a core mass much greater than the expected critical core mass of 10–20 M_\oplus (Mizuno 1980; Pollack et al. 1996), and thus nonetheless present a challenge to standard core-accretion theory.

The planet is noteworthy in another respect. Observations by the *Spitzer Space Telescope* (Harrington et al. 2007) have shown the planet to have a dayside 8 μm brightness temperature well in excess of its predicted blackbody temperature, when it is assumed that all incident radiation is absorbed and subsequently re-emitted uniformly across the entire surface of the planet. Fortney et al. (2008) posit that highly irradiated planets such as HD 149026b, which they term “pM” class planets, will generally show bright day sides and large day/night temperature contrasts. They argue that the incident stellar flux is prominently absorbed by gaseous TiO and VO high in the atmospheres of pM planets where the radiative timescale is much shorter than the advective timescale (see also Hubeny et al. 2003; Burrows et al. 2008). This is in contrast to less irradiated “pL” planets where Ti and V are expected to largely condense out of the atmosphere, permitting the stellar flux to be absorbed deeper in the atmosphere where the two timescales are comparable. Hence, it is only for the pL class that a heated parcel of gas is able to be advected to the night side prior to cooling, resulting in similar day/night temperatures.

HD 149026b is thus a valuable case study for modelers of planetary atmospheres, structure, and formation. Unfortunately, the system is observationally challenging: the transit depth (3 mmag in V) is a factor of two shallower than any other presently known transiting planet, and more importantly, there are few adequate comparison stars nearby on the sky. The result is that the present fractional uncertainty in the key observable parameter, the planetary radius R_p , is 7% (Winn et al. 2008). This uncertainty is one of the largest among the ensemble of transiting planets. The state of uncertainty is unfortunate given that R_p is the essential constraint on models of the planet’s interior structure. Fortunately there is further scope for improvement through high-precision photometry.

This study is inspired by the potential of infrared photometry with *Spitzer* to reduce the uncertainty in R_p . While ground-based photometry suffers from significant levels of systematic noise when there are few good comparison stars, *Spitzer* has demonstrated 0.1 mmag photometry without any comparison stars (e.g., Knutson et al. 2007). Additionally, because of the near absence of stellar limb darkening in the infrared, transit light curve modeling is simplified and gives results largely independent of assumptions about limb-darkening coefficients. Previously, Sato et al. (2005), Charbonneau et al. (2006), and Winn et al. (2008, hereafter W08) have presented ground-based photometry of HD 149026. In this paper, we report *Spitzer* 8 μm observations of the transit of HD 149026b, and combine this with the previously published data in order to derive precise constraints on the properties of HD 149026b. In Section 2 we describe the observations and data reduction and in Section 3 we describe our analysis of the *Spitzer* light curve. In Section 4 we estimate the physical parameters of the HD 149026 system. We conclude with a discussion of the implications of our revised estimate of the planet radius for models of the interior structure of HD 149026b.

2. OBSERVATIONS AND REDUCTION

We observed the transit of HD 149026 on UT 2007 August 14, using the 8 μm channel of the IRAC instrument (Fazio et al. 2004) aboard *Spitzer* (Werner et al. 2004). The system was

⁵ Alfred P. Sloan Research Fellow.

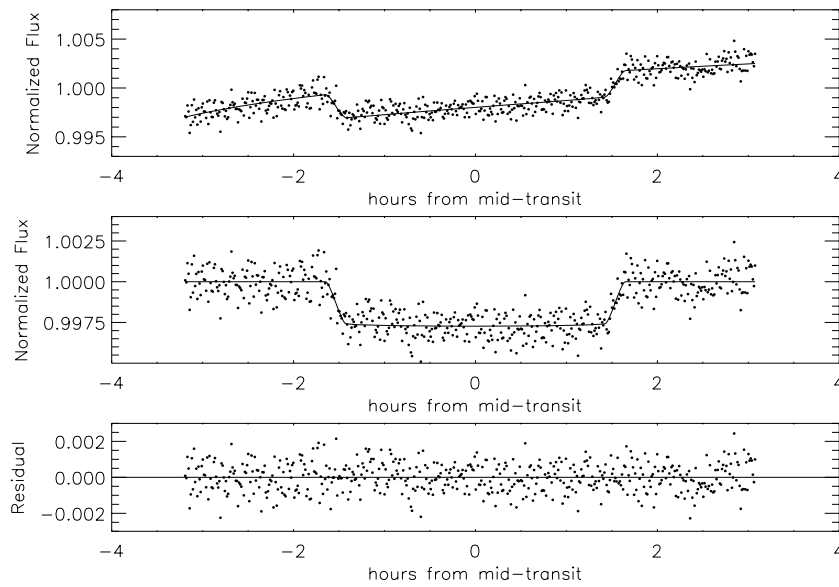


Figure 1. Transit photometry for HD 149026, with 40 s resolution (bins of 100 images). The top panel displays the raw light curve and the middle displays the light curve corrected for the detector ramp as described in Section 3. At the bottom are the residuals from the best-fit light curve.

observed at a 0.4 s cadence using IRAC’s 32 by 32 pixel sub-array mode, in which frames of 64 images are taken in rapid succession. Over the course of our observations, we obtained 1047 such frames, resulting in 67,008 total images. Our observational strategy matches that of recent *Spitzer* observations of HD 189733 and GJ 436 (e.g., Knutson et al. 2007; Deming et al. 2007; Gillon et al. 2007); the telescope positioning was held fixed to avoid time loss during telescope movements and to minimize errors from an imperfect flat-field correction. In the IRAC 8 micron channel, there is a well known rise in detector sensitivity during observational sequences (see e.g., Harrington et al. 2007; Knutson et al. 2007), which is steepest at the beginning of observations and asymptotes within several hours for highly illuminated ($> 250 \text{ MJy Sr}^{-1}$) pixels. We padded the beginning of our observational window so that the transit would begin nearly 3 hr into observations, thus avoiding the steepest part of this “ramp.”

In each image, we assessed the background flux by taking the median pixel value from the corner regions of each 32 by 32 image. We performed aperture photometry, settling on a 3.5 pixel aperture radius, for which the rms of the time series is minimized. From the time stamp reported for each frame of 64 0.4 s exposures, we calculated the Julian Date (JD) of the center of integration for each image. We applied the heliocentric correction to the JD using the position of *Spitzer* obtained from the JPL Horizons Ephemeris System. In each series of 64 images there is a well known effect, with the first 5–10 and 58th images showing anomalously low star fluxes and background levels (see e.g., Harrington et al. 2007). Background subtraction generally corrects for this effect, but we elected to drop the 1st image from each series of 64, because the background levels in these images exhibit more dispersion than in the other images. We trimmed the first 45 minutes of data, when the ramp is steepest. We flagged images when the star centroid, calculated with a flux-weighted average, was 4σ away from the median centroid position. Such 4σ centroid deviants were generally caused by cosmic rays or other contamination in the photometric aperture. We further flagged images when the flux measurement was 4σ from a smoothed (binned) light curve, or the background level was 4σ from a binned time series of the background. We

flagged 317 images (0.5% of the total) according to the last three criteria.

3. SPITZER LIGHT CURVE ANALYSIS

One major benefit of observing transits at $8 \mu\text{m}$ is that stellar limb darkening has a small effect on the shape of the transit light curve. To determine its extent, we consulted a theoretical limb-darkening model (Kurucz 1979, 1994) for a $T_{\text{eff}} = 6250 \text{ K}$, $\log g = 4.5$, $[\text{Fe}/\text{H}] = 0.3$ star at $\lambda = 8 \mu\text{m}$. We fit this model⁶ to the Claret (2000) four parameter nonlinear limb-darkening law (see also Beaulieu et al. 2008 for a similar handling of limb darkening). Though the limb darkening is indeed modest, we find that incorporating it in our light curve modeling (described below) leads to non-negligible changes in the best-fit parameters and a reduction in the best-fit χ^2 by more than 1. We modeled the light curve using the “small-planet” transit routine of Mandel & Agol (2002). The small planet approximation is not usually suitable for analyzing high quality transit data, especially for systems with large planet–star radius ratios ($R_p/R_\star \gtrsim 0.1$), but here we find the approximation leads to insignificant changes in the best-fit parameters (due to the very small planet–star radius ratio of HD 149026). We assumed a circular orbit, which is expected from tidal dissipation and supported by current radial velocity data (e.g., Sato et al. 2005). We parametrized the light curve with four geometric parameters that are independent of prior assumptions on the stellar properties: the planet–star radius ratio R_p/R_\star , the stellar radius to orbital radius ratio R_\star/a , the inclination i , and the time of mid-transit T_c . To correct for the ramp and other possible detector effects, we adopted a correction factor $f = (c_0 + c_1 \log(t - t_0) + c_2 \log^2(t - t_0))$, where t_0 was fixed to a time a few minutes before the first observations. Note that in all of our modeling below, we fit for the detector correction coefficients simultaneously with the transit-related parameters, allowing us to take into account how changes in the correction coefficients may impact the transit parameters.

We performed a least-squares fit to our unbinned data over the seven parameter space ($R_p/R_\star, R_\star/a, i, T_c, c_0, c_1, c_2$), using an IDL implementation of the amoeba algorithm (e.g. see Press

⁶ See <http://kurucz.harvard.edu/grids/>.

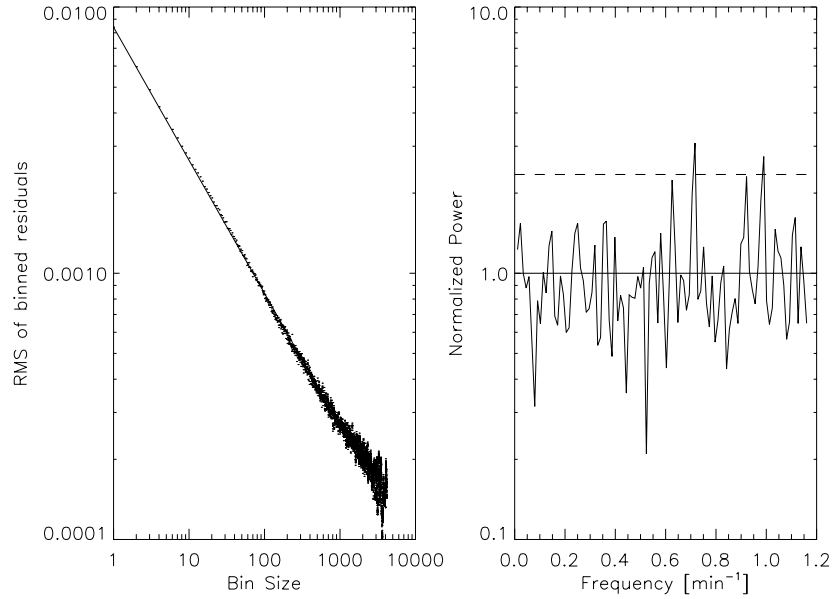


Figure 2. Left: root-mean-square of binned residuals vs. bin size. The solid line is proportional to $N^{-1/2}$ and is normalized to match the value for bin size $N = 1$. Right: power spectrum estimate for the time-series residuals. The estimate has been divided by the power spectrum expected for randomly generated white noise of the same standard deviation and time sampling as the *Spitzer* data. The dashed line represents the median peak value of the simulated power spectrum estimates.

et al. 1992). The data, corrected for the ramp and binned 100:1 are shown in Figure 1, together with this best-fitting solution. To understand the level of photometric noise and its properties, we examined the residuals from this best fit. We determined a normalized rms residual of 8.3×10^{-3} , only 15% greater than the expected photon noise. We found that the level of photometric noise was constant over the duration of the observations, and furthermore that the noise was essentially “white.” In the left panel of Figure 2 we show that the scatter in binned residuals decreases with bin size as $N^{-1/2}$ for bins of up to 1000 images. In the right panel of Figure 2, we display a power spectrum estimate for the time series of residuals. To compute this, we first binned the residuals for each frame of 64 images. This step creates an evenly spaced time series of 940 residuals because IRAC, in sub-array mode, takes exposures in sets of 64 images (once every 25.6 s). This binning also avoids having to interpolate over gaps caused by flagged images. Though binning removes the highest frequency information from the spectrum, we are less concerned with noise power on the affected timescales, which are shorter than the other timescales relevant in a transit light curve (e.g., the ingress/egress duration). We estimated the power spectrum via the (modulus squared) discrete Fourier transform. To reduce the variance at each frequency, we smoothed with a seven point “Daniell,” or moving average, filter. We compared our power spectrum estimate with that expected of white noise by simulating 10^5 time series with identical, independent Gaussian deviates of the same time sampling and standard deviation as the *Spitzer* residuals. We note that 5% of the simulated power spectra show peak values as high as the peak value in *Spitzer* power spectrum, while two peaks in the *Spitzer* power spectrum exceed the median peak value of the simulated spectra (the dashed line in Figure 2).

Because of the light curve modeling degeneracy between the parameters a and R_* , transit photometry alone cannot determine the quantity of interest, R_p . To break this degeneracy, one can either apply an external constraint on a (typically via Newton’s version of Kepler’s Third Law and a constraint on M_*), on R_* , or on some combination of both. Before applying any such constraints, we estimated the probability distributions for the

seven light curve parameters by using the widely employed Markov Chain Monte Carlo (MCMC) technique (see e.g., Tegmark et al. 2004; Winn et al. 2007; Burke et al. 2007). The benefit of performing this analysis without any a priori assumptions on stellar quantities is that we can compare, on equal footing, the light curve constraints derived from our data with constraints derived from other photometric data. For this analysis, we adopted a conventional χ^2 function as our goodness-of-fit statistic:

$$\chi^2 = \sum_i \left(\frac{f_{\text{mod}}(i) - f_{\text{obs}}(i)}{\sigma} \right)^2 \quad (1)$$

where $f_{\text{mod}}(i)$ is the calculated flux at the time of the i th data point, $f_{\text{obs}}(i)$ is the i th flux measurement, and σ is fixed to the value of the rms determined in the previous paragraph. We produced 10 chains of length 10^6 , with each chain starting from independent parameter points randomly chosen from a broad region (spanning approximately 5σ) in parameter space. The initial 25% of each chain was trimmed and the 10 chains were concatenated. We found that the Gelman–Rubin R statistic was less than 1.01 for each parameter, which is an indication of convergence.

Our MCMC analysis yields $R_p/R_* = 0.05158 \pm 0.00077$ and impact parameter $|b| \equiv |a \cos i/R_*| = 0.62_{-0.24}^{+0.08}$. Our result for R_p/R_* is larger than that of W08 ($R_p/R_* = 0.0491_{-0.0005}^{+0.0018}$), though the difference is only modestly significant. Our result for $|b|$ is higher than that of W08 ($|b| = 0.00$ with 68% upper limit $|b| = 0.36$). We expect that our R_p/R_* result is more robust than the result from the optical data because, for weakly limb-darkened infrared light curves, the radius ratio is measured almost directly from the observed flux decrement. For optical light curves, however, the radius ratio is strongly covariant with the assumed limb-darkening coefficients. That is, an error in the assumed limb darkening can translate into an error in the radius ratio. To investigate this point, we conducted a comparison with previously published $(b + y)/2$ HD 149026 light curves of Sato et al. (2005) and W08 (see Section 4.2 for further discussion of these data). For this sub-study we modeled the data in a manner

Table 1
Estimates of the HD 149026 System Parameters

Parameter	Median	15.9th Percentile	84.1st Percentile
R_p/R_* ^a	0.05158	-0.00077	+0.00077
R_p/R_*	0.05147	-0.00077	+0.00076
i [deg] ^a	85°:4	-1°:9	+2°:5
i [deg]	85°:3	-0°:8	+0°:9
a/R_* ^a	6.23	-0.63	+0.71
a/R_*	6.20	-0.25	+0.28
ρ_* [g cm ⁻³] ^a	0.51	-0.13	+0.21
ρ_* [g cm ⁻³]	0.547	-0.064	+0.076
$\log g_p$ [cgs] ^{a,b}	3.18	-0.09	+0.10
$\log g_p$ [cgs] ^b	3.203	-0.048	+0.049
P [days]	2.8758887	-0.0000035	+0.0000035
T_c [HJD] ^a	2454327.37213	-0.00050	+0.00050
R_p [R_J]	0.755	-0.040	+0.040
R_* [R_\odot]	1.497	-0.069	+0.069

Notes.

^a Determined from analysis of *Spitzer* data alone.

^b Using $K = 43.3 \pm 1.2 \text{ m s}^{-1}$, from Sato et al. (2005).

similar to that above, but assumed a linear limb-darkening coefficient, which we allowed to vary freely. For the optical light curves, we determined a correlation coefficient between R_p/R_* and the limb-darkening coefficient of $r = 0.55$, while for the same experiment with the *Spitzer* data we found a much weaker correlation ($r = -0.20$). Furthermore, in the presence of strong limb darkening, the radius ratio and impact parameter are also correlated; the radius ratio can be traded off with the impact parameter to produce similar transit depths. We point this out because it suggests that the above mentioned discrepancies for b and R_p/R_* are in fact correlated with each other.

The results for these parameters and other important transit observables are reported in Table 1 (marked with a superscript ‘a’). Noteworthy are the results for the mean stellar density, ρ_* , and planet surface gravity, g_p , which are model-independent determinations making use of information only from transit photometry and Doppler measurements (Seager & Mallén-Ornelas 2003; Southworth et al. 2007; Sozzetti et al. 2007). We also find $a/R_* = 6.23^{+0.71}_{-0.63}$, which is consistent with the determination of W08 ($a/R_* = 7.11^{+0.03}_{-0.81}$). Note that the corresponding fractional uncertainty in our result for R_*/a is fairly large ($\simeq 10\%$).

4. STELLAR AND PLANETARY PROPERTIES

In the transit modeling literature, the parameter of interest, R_p , is usually determined via one of the following two methods. In the first, one obtains an externally determined value of R_* , and then multiplies it by the light curve results for R_p/R_* . In the second, one assumes a value for M_* , utilizes Newton’s version of Kepler’s third law to derive the semimajor axis, a , and then applies the light curve results for R_*/a (and R_p/R_*).⁷ While the first method has the advantage that transit photometry determines R_p/R_* more precisely than R_p/a , the resulting R_p depends strongly on the assumed R_* ($R_p \propto R_*$). This method also has the disadvantage of effectively disregarding any information gleaned from the light curve on R_*/a . In the second method, the result for R_p depends only weakly on the assumed M_* ($R_p \propto M_*^{1/3}$), but, in our case, R_p/a is

not constrained well enough to lead to a satisfactorily precise determination of R_p . For these reasons, we adopt a hybrid approach, imposing a radius constraint and, to make use of the R_*/a information, a mass constraint. Though the addition of this mass constraint represents an increased dependence on stellar models, we consider it a fairly benign dependency given how weakly the mass enters into the transit modeling ($\propto M_*^{1/3}$).

In this section, we augment the *Spitzer* dataset with ten previously published light curves. Together with independent constraints on the stellar properties described below, we fit for the R_p and other planet and stellar quantities.

4.1. Stellar Radius and Mass

Using a collection of interferometric angular diameter measurements, Kervella et al. (2004) derived empirical relations for the angular diameters of dwarf stars as a function of Johnson magnitudes. We use their V , K relation for the angular diameter, ϕ (mas),

$$\log \phi = 0.0755(V - K) + 0.5170 - 0.2K. \quad (2)$$

Kervella et al. (2004) found the rms residual from this best-fit relation to be less than 1% for 20 stars ranging from spectral type A0 to M2. We applied $V = 8.15$, as found in the *Hipparcos* Catalog, and $K = 6.85$, after transforming the 2MASS K_s magnitude to Johnson K following Carpenter (2001). After propagating the uncertainties in the photometry and Kervella et al. (2004) best-fit parameters, we determined $\phi = 0.1755 \pm 0.0021 \text{ mas}$ (see also Torres et al. 2008). The formal uncertainty in angular diameter is thus 1% and negligible compared to the uncertainty in parallax. After combining with the re-reduced *Hipparcos* parallax and uncertainty ($\pi = 12.59 \pm 0.70$) of van Leeuwen (2007), we determine $R_* = 1.50 \pm 0.09 R_\odot$. For the stellar mass, we adopt the value $M_* = 1.30 \pm 0.10 M_\odot$ from Sato et al. (2005), who derived the value by matching stellar evolution tracks to spectroscopic properties.

4.2. Light Curve Analysis Revisited

We simultaneously fitted our *Spitzer* data together with three light curves published by Sato et al. (2005), two light curves by Charbonneau et al. (2006) and five light curves by W08. The ten previous transit observations are discussed in detail in the references above, but we describe them briefly here. The Sato et al. 2005 and W08 observations were obtained with 0.8 m automated photometric telescopes at the Fairborn Observatory. Fluxes were measured simultaneously through Strömgren b and y filters and averaged to create $(b+y)/2$ fluxes. The Charbonneau et al. (2006) observations were obtained with the Fred Lawrence Whipple Observatory 1.2 m telescope through the Sloan g and r filters. In analysis of the ten light curves, W08 divided each raw light curve by a linear function of time that was fitted to the out-of-transit data. This step corrects for airmass effects and other systematic trends, but also has the effect of normalizing each light curve to have unit mean out-of-transit flux. We adopted these corrected data as well as their revised photometric errors, which were rescaled to account for the effects of noise correlation on ingress/egress timescales. Note that the composite of these ten light curves, when binned to 30 s resolution, shows roughly the same scatter ($\sim 0.9 \text{ mmag}$) as the *Spitzer* data binned to the same resolution.

Next, we revisited the MCMC analysis of Section 3. We modeled the light curves as before, using the small-planet transit

⁷ Another possible route is to assume a stellar mass–radius relation (Cody & Sasselov 2002). We have chosen not to make such an assumption because of the uncertainty in the age and evolutionary state of HD 149026.

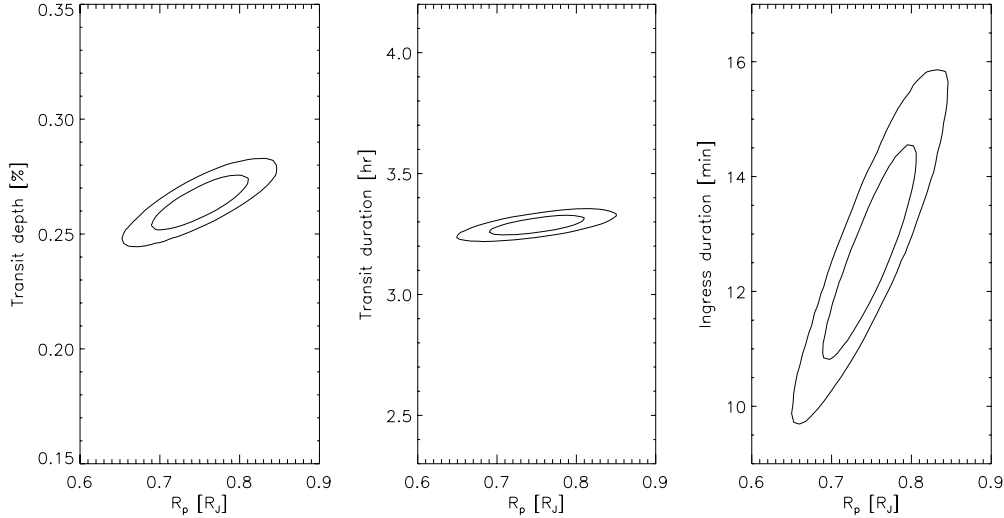


Figure 3. Joint posterior probability distributions for R_p and directly observable quantities, as estimated by the MCMC analysis described in Section 4. The contours mark the 68% and 95% confidence regions. Left: joint distribution for R_p and the “transit depth,” $(R_p/R_*)^2$. Middle: joint distribution for R_p and the transit duration, defined as the interval from 1st to 4th contact. Right: joint distribution for R_p and the ingress (egress) duration, defined as the interval from 1st to 2nd (3rd to 4th) contact. Note that the vertical axes in each panel are scaled so that they encompass roughly the same fractional variation.

routine of Mandel & Agol (2002). For the g and r band data, we assumed linear limb darkening, with coefficients as tabulated by Claret (2004) for a 6250 K, $\log g = 4.5$, and $[\text{Fe}/\text{H}] = 0.3$ star. For the $(b+y)/2$ data, we assumed a linear limb-darkening coefficient of 0.712, the average of Claret (2000) b and y limb-darkening coefficients, following W08. We employed nine free parameters: R_p/R_* , i , c_0 , c_1 , c_2 , P , T_c , M_* , and R_* , where the ramp correction coefficients, c_i , apply only to the *Spitzer* data. Note that we fit for only a single mid-transit time and required the transits to be spaced at integral multiples of P . W08 found no significant deviations from predicted transit times, so this is a reasonable assumption. We modified our goodness-of-fit statistic as follows:

$$\chi^2 = \sum_i \left(\frac{f_{\text{mod}}(i) - f_{\text{obs}}(i)}{\sigma} \right)^2 + \left(\frac{R_*/R_\odot - 1.50}{0.09} \right)^2 + \left(\frac{M_*/M_\odot - 1.30}{0.10} \right)^2 \quad (3)$$

with the second and third term reflecting the above determined stellar radius and mass with errors assumed to follow normal distributions. Note that the mass and radius constraints have entered into the χ^2 in a simple additive form, which is strictly valid only if the constraints were determined entirely independent of each other. In fact, the mass determination of Sato et al. (2005) makes use of the parallax, which implies that the mass and radius determinations have some level of intrinsic covariance. To examine the impact of this covariance, we repeated our analysis with the following trial goodness-of-fit statistic,

$$\chi_{\text{trial}}^2 = \sum_i \left(\frac{f_{\text{mod}}(i) - f_{\text{obs}}(i)}{\sigma} \right)^2 + \frac{1}{1 - \rho_{MR}^2} \times \left[\left(\frac{R_*/R_\odot - 1.50}{0.09} \right)^2 + \left(\frac{M_*/M_\odot - 1.30}{0.10} \right)^2 - 2\rho_{MR} \left(\frac{R_*/R_\odot - 1.50}{0.09} \right) \left(\frac{M_*/M_\odot - 1.30}{0.10} \right) \right], \quad (4)$$

where we experimented with values of the correlation coefficient, ρ_{MR} , between -1 and 1 . For $-0.7 < \rho_{MR} < 0.7$, we found the best-fit parameters and error bars to be negligibly affected by the correlation, and we found the results were significantly impacted only when $|\rho_{MR}| > 0.9$. Since we expect the covariance between the stellar mass and radius determination to be more modest, we conclude that our results are not impacted by neglecting the covariance.

We conducted the analysis as before; we produced ten Monte Carlo chains of length 10^6 , cut the first 25% of each chain, and then combined the chains. For each parameter the Gelman–Rubin R statistic was well within 1% of unity. In Table 1, we report best-fit values and uncertainties for various parameters. We take the best-fit value to be the median of the MCMC samples, and for the uncertainties, we report the interval that encloses the central 68.3% of the MCMC samples.

We determine a stellar radius of $1.497 \pm 0.069 R_\odot$, which is moderately refined compared to its prior distribution ($1.50 \pm 0.09 R_\odot$). This refinement indicates that the combination of *Spitzer* and ground-based data is able provide some statistical influence on the parameter estimation through the observational constraint on R_*/a . We note that the external stellar radius constraint reinforces the high impact parameter solutions favored by the analysis of Section 3 (*Spitzer* data alone). This arises because the radius constraint favors relatively large stellar radii, which, for the given observed transit duration, can only be accommodated by non-equatorial impact parameters. The planet radius is determined to be $0.755 \pm 0.040 R_J$, with an uncertainty that is reduced versus previously published determinations (for example, $0.71 \pm 0.05 R_J$ as determined by W08). The reduction is partly due to the smaller uncertainty in the revised *Hipparcos* parallax (van Leeuwen 2007) that we have adopted, and partly due to the combination of the *Spitzer* and ground-based data.

In Figure 3, we look deeper into the observational constraints on the key parameter, R_p . The most directly observable quantities from a transit light curve are the transit depth, the total transit duration, and the ingress or egress duration; a measurement of these three observables is sufficient (at least in the absence of limb darkening) to determine the more physical parameters R_p/R_* , R_*/a , and $\cos i$. By examining the joint posterior distributions for the three observables with the parameter R_p , one can

gain insight into the current observational limitations on the precision of R_p . While each of the panels in Figure 3 demonstrates covariances, the third panel (R_p and ingress duration) shows particularly strong covariance. Thus, the major limiting factor in reducing the uncertainty in planetary radius appears to be the ability to resolve the ingress duration. Unfortunately, constraining this quantity with ground-based photometry is complicated by limb darkening and the effects of systematics and correlated errors (e.g., Pont & Moutou 2007).

4.3. Influence of Star Spots

As with limb darkening, an inhomogeneous surface brightness due to spots would impact both the depth and shape of the transit light curve. If the transit chord intersects a star spot, a positive “bump” will be introduced into the transit light curve, while if the transit chord is along an unspotted area of an otherwise spotted star, the transit would appear deeper (see e.g. Knutson et al. 2009; Beaulieu et al. 2008). The existence of star spots can be investigated by long-term photometric observations of the star, monitoring for periodic flux variations.

Previously published APT data has shown HD 149026 to be photometrically stable to 0.0015 mag, the limit of precision of the APTs (Sato et al. 2005). Further $(b + y)/2$ out-of-transit observations have been obtained with the APTs, extending the dataset to over three years (Winn et al. 2008; G. Henry 2008, private communication). With this additional APT data, kindly shared with us by G. Henry, we have searched for evidence of star spot-induced variability. We computed the periodogram for the time series (550 total flux measurements) in fine steps of the period for periods between 0.5 and 100 days. Examination of all prominent peaks in the periodogram reveals no evidence for any significant periodicities, and allows us to place an upper limit on the peak-to-peak amplitude of any sinusoid (in the period range 0.5–100 days) of less than 0.001 mag. Any spots at or below this level will have negligible impact on the transit light curve, especially given that the 1σ uncertainty in the transit depth for HD 149026b is 3%.

4.4. Refined Ephemeris

The precise transit timing from Section 3, along with the fact that the *Spitzer* light curve extends the time base-line of HD 149026b transit observations, enables a significant refinement in the transit ephemeris. For the previously published transit observations, we adopt the transit times and uncertainties listed in Table 3 of W08. We fit the timing data to the equation

$$T_c(E) = T_c(0) + E \times P \quad (5)$$

where T_c is the transit time, E is the transit epoch, and P is the orbital period. We determine $P = 2.8758887 \pm 0.0000035$ and $T_c(0) = 2454327.37211 \pm 0.00047$, with $\chi^2/N_{\text{dof}} = 0.564$, with $N_{\text{dof}} = 10$. In Figure 4, we show the transit time residuals for all published transits.

5. DISCUSSION

We have presented and analyzed *Spitzer* 8 μm transit observations of the HD 149026 system. By incorporating previously published data, and adopting constraints on the stellar mass and radius, we improve the determination of the planetary radius to $R_p = 0.755 \pm 0.040 R_J$. Our measurement reinforces previous findings of the intriguingly small radius of HD 149026b. To place this result in context, models in which HD 149026b

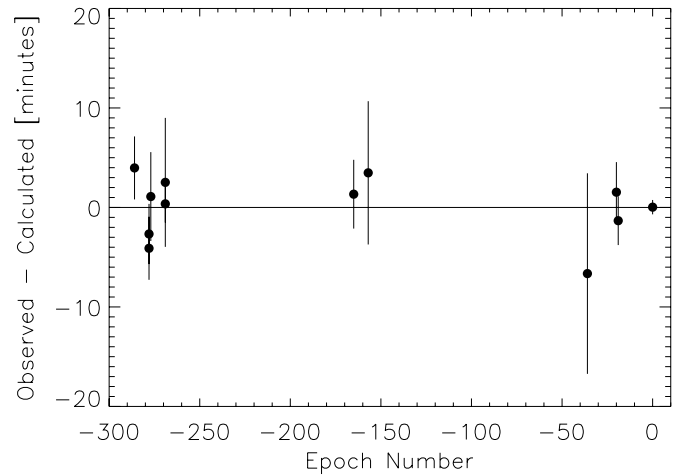


Figure 4. Observed minus calculated mid-transit times for HD 149026b. The calculated transit times are derived from the ephemeris in Equation (2). The estimates for the first 11 transit times are drawn from Table 3 of W08.

(with a total mass of $114 \pm 2 M_{\oplus}$) is composed purely of H/He require a radius greater than $1.1 R_J$ (e.g., Burrows et al. 2007).

The implications of the small measured radius on the interior structure of HD 149026b have been modeled by a number of authors. Most works (Sato et al. 2005; Fortney et al. 2006; Ikoma et al. 2006; Burrows et al. 2007) have assumed that all of the heavy elements reside within the planet’s core, although it was often stressed that this may not necessarily be the case. For instance, recent models of Jupiter’s structure indicate that the majority of its heavy elements are mixed within the H/He envelope (Saumon & Guillot 2004). Baraffe et al. (2008) recently computed evolution models of HD 149026b and other planets and showed that if these heavy elements are distributed within the envelope, rather than all in the core, less are needed to obtain the same model radius at a given age. However, Ikoma et al. (2006) also explored this effect, and noted that enhanced metallicity of the H/He envelope should also lead to higher atmospheric opacity, which will slow the contraction, necessitating more heavy elements.

The choices made by the modelers have been diverse, and many different atmospheric boundary conditions, assumed heat capacities of the heavy elements, and equations of state (EOSs) for the heavy elements have been explored. Interior heavy element mass estimates have generally ranged from 50–90 M_{\oplus} for a planet radius of $0.725 \pm 0.05 R_J$. On the low end, Ikoma et al. (2006) found that a 35 M_{\oplus} core would be necessary, if the planet cooled and contracted in isolation, then was brought to 0.042 AU at the present time. On the high end, Burrows et al. (2007) found 110 M_{\oplus} , if the planet has an atmospheric opacity 10 times larger than solar composition atmosphere models. For all of these models, uncertainty in the measured radius is more significant than the uncertainty in the system age.

A full exploration of new evolution models, including the potential contribution of TiO/VO opacity, which may be present in the planet’s visible atmosphere (Fortney et al. 2006; Fortney et al. 2008; Burrows et al. 2008), is beyond the scope of this paper. Given the previous modeling efforts, together with uncertainties in atmospheric metallicity and opacities and the distribution of heavy elements within the planet, the 50–90 M_{\oplus} heavy element mass range is still likely to be correct, even for our modestly larger measured radius. We note that current estimates of the heavy element abundance of Saturn (which is similar in mass to HD 149026b) and Jupiter range from 13–28 M_{\oplus} and

8–39 M_{\oplus} , respectively (Saumon & Guillot 2004). Uncertainty in the composition of giant planets is the rule, not the exception.

As has been stressed recently by Burrows et al. (2007), and others, constraints for any particular planet will remain uncertain, but with a large sample size of transiting planets at various masses, radii, orbital distances, and stellar metallicity, trends will emerge which will shed light on the formation and structure of these planets (Guillot et al. 2006; Fortney et al. 2007; Burrows et al. 2007).

We are grateful to F. van Leeuwen for providing parallax data for HD 149026, and to G. Takeda for discussions regarding the spectroscopic determination of stellar properties. We are especially grateful to G. Henry for sharing many seasons of photometric data. We would also like to thank an anonymous referee for specific and helpful recommendations. This work is based on observations made with the *Spitzer Space Telescope*, which is operated by the Jet Propulsion Laboratory, California Institute of Technology under a contract with NASA. Support for this work was provided by NASA through an award issued by JPL/Caltech.

REFERENCES

- Baraffe, I., Chabrier, G., & Barman, T. 2008, *A&A*, 482, 315
 Beaulieu, J. P., Carey, S., Ribas, I., & Tinetti, G. 2008, *ApJ*, 677, 1343
 Burke, C. J., et al. 2007, *ApJ*, 671, 2115
 Burrows, A., Budaj, J., & Hubeny, I. 2008, *ApJ*, 678, 1436
 Burrows, A., Hubeny, I., Budaj, J., & Hubbard, W. B. 2007, *ApJ*, 661, 502
 Carpenter, J. M. 2001, *AJ*, 121, 2851
 Charbonneau, D., et al. 2006, *ApJ*, 636, 445
 Claret, A. 2000, *A&A*, 363, 1081
 Claret, A. 2004, *A&A*, 428, 1001
 Cody, A. M., & Sasselov, D. D. 2002, *ApJ*, 569, 451
 Deming, D., Harrington, J., Laughlin, G., Seager, S., Navarro, S. B., Bownan, W. C., & Horning, K. 2007, *ApJ*, 667, L199
 Fazio, G. G., et al. 2004, *ApJS*, 154, 10
 Fortney, J. J., Lodders, K., Marley, M. S., & Freedman, R. S. 2008, *ApJ*, 678, 1419
 Fortney, J. J., Marley, M. S., & Barnes, J. W. 2007, *ApJ*, 659, 1661
 Fortney, J. J., Saumon, D., Marley, M. S., Lodders, K., & Freedman, R. S. 2006, *ApJ*, 642, 495
 Gillon, M., et al. 2007, *A&A*, 471, L51
 Guillot, T., Santos, N. C., Pont, F., Iro, N., Melo, C., & Ribas, I. 2006, *A&A*, 453, L21
 Harrington, J., Luszcz, S., Seager, S., Deming, D., & Richardson, L. J. 2007, *Nature*, 447, 691
 Hubeny, I., Burrows, A., & Sudarsky, D. 2003, *ApJ*, 594, 1011
 Ikoma, M., Guillot, T., Genda, H., Tanigawa, T., & Ida, S. 2006, *ApJ*, 650, 1150
 Kervella, P., Thévenin, F., Di Folco, E., & Ségransan, D. 2004, *A&A*, 426, 297
 Knutson, H. A., et al. 2007, *Nature*, 447, 183
 Knutson, H. A., et al. 2009, *ApJ*, 690, 822
 Kurucz, R. L. 1979, *ApJS*, 40, 1
 Kurucz, R. 1994, Solar Abundance Model Atmospheres for 0, 1, 2, 4, and 8 km/s CD-ROM 19 (Cambridge, MA: Smithsonian Astrophysical Observatory)
 Mandel, K., & Agol, E. 2002, *ApJ*, 580, 171
 Mizuno, H. 1980, *Progress of Theoretical Physics*, 64, 544
 Pollack, J. B., Hubickyj, O., Bodenheimer, P., Lissauer, J. J., Podolak, M., & Greenzweig, Y. 1996, *Icarus*, 124, 62
 Pont, F., & Moutou, C. 2007, Transiting Extrapolar Planets Workshop, 366, 209
 Press, W. H., Teukolsky, S. A., Vetterling, W. T., & Flannery, B. P. 1992, Numerical Recipes in Fortran 77: The Art of Scientific Computing (Cambridge, UK: Cambridge Univ. Press)
 Sato, B., et al. 2005, *ApJ*, 633, 465
 Saumon, D., & Guillot, T. 2004, *ApJ*, 609, 1170
 Seager, S., & Mallén-Ornelas, G. 2003, *ApJ*, 585, 1038
 Southworth, J., Wheatley, P. J., & Sams, G. 2007, *MNRAS*, 379, L11
 Sozzetti, A., Torres, G., Charbonneau, D., Latham, D. W., Holman, M. J., Winn, J. N., Laird, J. B., & O'Donovan, F. T. 2007, *ApJ*, 664, 1190
 Tegmark, M., et al. 2004, *Phys. Rev. D*, 69, 103501
 Torres, G., Winn, J. N., & Holman, M. J. 2008, arXiv:0801.1841
 van Leeuwen, F. 2007, in *Astrophysics and Space Science Library* 350, *Hipparcos, the New Reduction of the Raw Data*, ed. F. van Leeuwen, Institute of Astronomy, Cambridge University, & Cambridge, UK (Dordrecht: Springer), 20
 Werner, M. W., et al. 2004, *ApJS*, 154, 1
 Winn, J. N., Henry, G. W., Torres, G., & Holman, M. J. 2008, *ApJ*, 675, 1531
 Winn, J. N., Holman, M. J., & Roussanova, A. 2007, *ApJ*, 657, 1098